Edge effects in molybdenum-encapsulated molten silicate shock wave targets

Gregory Hale Miller, and Elbridge Gerry Puckett

Citation: Journal of Applied Physics **75**, 1426 (1994); doi: 10.1063/1.356424
View online: https://doi.org/10.1063/1.356424
View Table of Contents: http://aip.scitation.org/toc/jap/75/3
Published by the American Institute of Physics

Edge effects in molybdenum-encapsulated molten silicate shock wave targets

Gregory Hale Miller
Department of the Geophysical Sciences, University of Chicago, 5734 South Ellis Avenue, Chicago, Illinois 60637

Elbridge Gerry Puckett
Department of Mathematics and Institute of Theoretical Dynamics, University of California, Davis, California 95616

(Received 19 July 1993; accepted for publication 20 October 1993)

The customary acoustic calculation used to design shock wave equation of state targets may be inapplicable when the sample is enveloped in a container that has a higher shock impedance than the sample being studied. In this case the edge effect is compressional, and could travel faster than the speed of sound. We present computations of the nonlinear wave interactions that occur at the sample-container interface of molybdenum-encased molten silicate shock wave targets. In all cases considered here, the edge effect is acoustic despite the higher shock impedance of the container. The computational method is an extension of a conservative Eulerian finite difference scheme for two materials in two dimensions that is based on a second-order Godunov method. This new method includes adaptive mesh refinement, a volume-of-fluid interface tracking algorithm, and a Mie-Grüneisen equation of state to describe liquids and solids in the hydrostatic limit.

I. INTRODUCTION

Shock waves have been used as an experimental technique for determining equations of state at very high pressure for over 40 years.[1] In such experiments, a shock is typically created by the impact of an explosively driven plate of some reference material against a plate of the sample being studied. The impact velocity and the resulting shock wave velocity are measured, and transformed into a pressure, density, and internal energy determination by application of the one-dimensional Rankine-Hugoniot conservation laws.[2–4] By this general methodology, equations of state have been determined to pressures as high as several TPa.[5] These equations of state are essential for using seismic data to constrain the chemical and mineralogical structure of the Earth. Such data are also used to calibrate secondary pressure standards, such as the ruby fluorescence pressure scale that is widely used in diamond anvil cell experiments.[6,7]

In actual practice, the one-dimensional Rankine-Hugoniot relations will be applicable only over some small region of the sample assembly, if at all. This is because edge effects, usually in the form of adiabatic release waves, spoil the one-dimensional geometry. The proper design of a shock wave sample must take this into consideration. This is normally done by application of an argument given by Al'tshuler *et al.*[8] (Fig. 1). An acoustic disturbance is generated at the edge or corner of the sample. This disturbance travels at the sound speed c in the shocked material, which itself flows at velocity U_P, the particle velocity. The intersection of this acoustic disturbance with the shock front (velocity U_S) sweeps out a cone whose angle α with the normal to the shock front is given by:

$$U_S^2 \tan^2\alpha = c^2 - (U_S - U_P)^2. \tag{1}$$

The aspect ratio of a well-designed shock sample is chosen to guarantee that the apex of the cone lies outside the sample, i.e., the ratio of target radius R to thickness H should satisfy $R > H \tan\alpha$ (Fig. 1). If the apex lies within the sample, and the shock is detected only at the sample's surface, then the shock will not be planar where measurable, the one-dimensional Rankine-Hugoniot equations will not be applicable, and the experiment will be uninterpretable.

In general, the quantities needed to evaluate (1) are not known in advance. The Hugoniot equation of state itself, which can be expressed $U_S = f(U_P)$, is often what is sought in the experiment. The sound speed c is also generally unknown. In fact, Al'tshuler *et al.* used measurements of the angle α as a method of determining the high pressure sound speed in shocked solids.

More complex sample assemblies than that depicted in Fig. 1 are required when the sample is a liquid. Then, it is most convenient to encapsulate the sample in a solid container. Disturbances that break the one-dimensional symmetry of the original shock will again be generated at the corners of the sample, including the sample-container interface. If the shock impedance of the container is lower than that of the sample, the signal will again be an acoustic one, and the Al'tshuler *et al.* method will be applicable for determining the minimum aspect ratio. As a rule, however, solids have higher shock impedances than liquids. The signal generated at the liquid-solid interface might therefore be propagated as an oblique shock at a velocity that is greater than the high-pressure sound speed. If this is the case the Al'tshuler *et al.* method of calculating α would not be appropriate, and measurement of the angle α would not yield the sound speed through (1).

In this study we are particularly interested in characterizing the edge effects present in experiments designed to

 0021-8979/94/75(3)/1426/9/$6.00

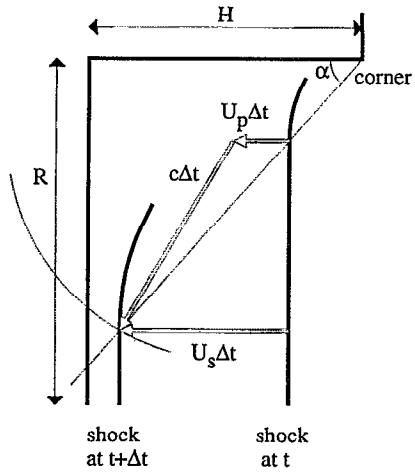

FIG. 1. Edge effect from a corner after Al'tshuler *et al.* (Ref. 8).

measure the equation of state of molten silicates.[9–13] In those experiments the target assemblies [Fig. 2(a)] consist of a molybdenum container, which also serves as an induction furnace element, surrounding a liquid sample. The molybdenum walls were sufficiently thick that their impact on the edge effects cannot be dismissed *a priori*. The shock impedance of molybdenum is considerably larger than that of the molten sample; thus the first edge signal propagated inward is compressive, and could travel faster than the speed of sound.

To characterize the edge effects in those experiments, we present models for the problem of an initially planar shock hitting a corner between two different materials. This corresponds to the earliest time behavior of the experiment shown in Fig. 2(a), which will suffer additional complications when the rarefaction fan generated at the outer circumference of the target has penetrated the outer wall of the assembly. Although the details of the interaction of that rarefaction fan with the flow fields generated by the sample-wall interaction may also be complicated, the

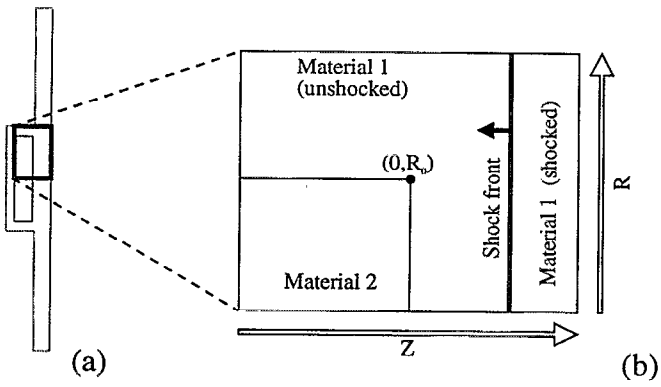

FIG. 2. (a) Sample design for molten silicate shock experiments. The target assembly consists of a molybdenum container surrounding a molten silicate sample. The assembly is impacted from the right, and the shock arrival times are detected on the left surfaces. Approximate dimensions are 6 by 45 mm. (b) Simplified geometry modeled here.

inward velocity of the leading edge of that rarefaction disturbance will not exceed the high-pressure sound speed of the sample materials. If in the limit of a very thick wall the Al'tshuler *et al.* rule remains valid, then it will also be valid for any wall thickness. Therefore, to test the applicability of the Al'tshuler *et al.* rule to the experiment shown in Fig. 2(a), we may consider the simplified geometry of Fig. 2(b). This is much simpler to model since it allows us to neglect the vacuum that surrounds the assembly. Success of the Al'tshuler *et al.* rule for our simplified model implies success of that rule for the actual experiments. A failure of the Al'tshuler *et al.* rule, however, does not necessarily imply its failure for the actual experiments. Additional computations with a more realistic geometry would then be required.

Because of the cylindrical symmetry of the experimental assemblies [Fig. 2(a)], the compressional edge effect signal will be focused as it travels toward the axis of symmetry. That focusing effect leads to a steepening of the compressional waves. Therefore, simple compressional wave systems computed in Cartesian coordinates that have not steepened into shocks might do so in cylindrical coordinates because of this focusing effect. Voinovich *et al.*[14] obtained a numerical solution to our problem [Fig. 2(b)], but for the case of ideal gases, and using Cartesian coordinates. The shock speed of the gas inside their corner is faster than that outside the corner: the opposite of our situation. They interpret their results to suggest that the leading disturbance in their slow material is propagated as an oblique shock even without the focusing effect of the experimental cylindrical geometry. Our computations are in cylindrical coordinates except where we illustrate the self-similarity of our results.

The simplified problem [Fig. 2(b)] involves the interaction of two wave systems. First, a *regular refraction* will occur at the material interface where it is parallel to the incident shock. The solution to this problem is simple. For all cases considered here, it will be a planar transmitted shock and a planar reflected rarefaction fan.[15] Second, an *"anomalous refraction"* will occur at the material interface where it is perpendicular to the incident shock. Anomalous refraction[16–19] refers to a refraction regime in which the angle between the material interface and the incident shock is greater than the Al'tshuler *et al.* angle α. When that occurs, the flow regime at the material interface influences the surrounding regions with acoustic waves, and the resulting wave topology can be quite complex.

In order to study this problem we have adapted a high resolution Eulerian finite difference gas dynamics program to handle condensed phases. The equation of state computation and the multifluid algorithm[20,21] required substantial revision for our problem. The multifluid algorithm described in Refs. 20 and 21, while presented in general thermodynamic terms, embodies assumptions that are clearly best suited to ideal gas equations of state. We modified those parts of the algorithm that embodied implicit ideal gas behavior, but left the underlying algorithmic structure unchanged. A brief summary of the overall program, with

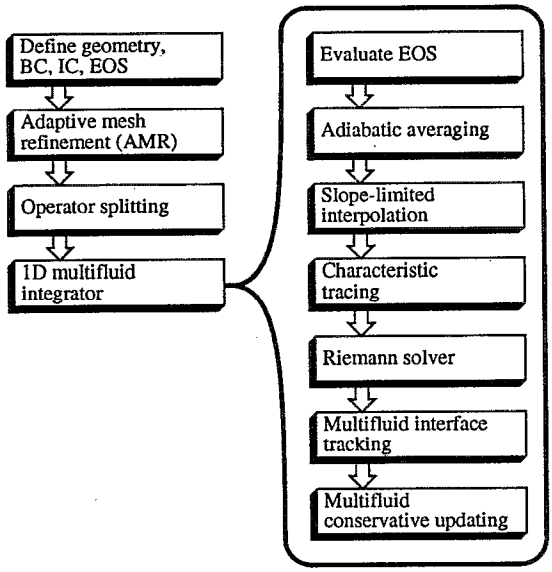

FIG. 3. Flowchart of computational methods.

emphasis on our modifications, follows. A more detailed description of our algorithm will be presented elsewhere.

II. COMPUTATIONAL METHOD

The overall structure of our program is shown in Fig. 3. At the heart of the algorithm is a routine for solving the so-called Riemann problem in one dimension (e.g., Ref. 22). It is assumed that two uniform regions called the left and right states, each possibly having a different pressure P, internal energy E, density ρ, velocity U, and equation of state, begin in contact with each other at the origin x_0 at time t_0. The essential feature of each of the five possible outcomes of this simple scenario is that they can be described as piecewise continuous regions separated by waves of constant velocity. The Riemann solver determines which of the five combinations of shock waves and/or rarefaction waves describe the solution, determines the velocities of the characteristic waves that bound each region of the solution, and finds the pressure, density, internal energy, and velocity of that region of the solution that exists at a specified point x for $t>t_0$.

Because our equation of state model is of the Mie-Grüneisen form,[23]

$$P(\rho,E)=P_H(\rho)+\rho\gamma(\rho)[E-E_H(\rho)], \tag{2}$$

and uses a Hugoniot reference state $[P_H(\rho),E_H(\rho)]$, it is convenient to approximate the equation of state in the Riemann problem as having a linear Hugoniot form. That is, we assume shock velocity U_S and particle velocity U_P, centered at an arbitrary state $(\rho,E,U=0)$, are related through:

$$U_S=c+sU_P. \tag{3}$$

Here, c is the bulk sound speed

$$c=\sqrt{\frac{K_S}{\rho}}, \tag{4}$$

and s is related to the pressure derivative of the adiabatic bulk modulus K_S through

$$s=\frac{1}{4}(1+K_S'), \tag{5}$$

each evaluated at the reference state (ρ,E). The adiabatic bulk modulus K_S and its adiabatic pressure derivative K_S' are obtained by differentiation of (2):

$$K_S(\rho,E)\equiv\rho\left.\frac{\partial P}{\partial\rho}\right|_S=\rho\frac{\partial P}{\partial\rho}+\frac{P}{\rho}\frac{\partial P}{\partial E}, \tag{6}$$

$$K_S'(\rho,E)\equiv\left.\frac{\partial K_S}{\partial P}\right|_S$$
$$=\left[\rho\frac{\partial P}{\partial\rho}+\rho^2\frac{\partial^2 P}{\partial\rho^2}+\frac{\partial P}{\partial\rho}\frac{\partial P}{\partial E}+2P\frac{\partial^2 P}{\partial\rho\partial E}-\frac{P}{\rho}\frac{\partial P}{\partial E}+\frac{P^2}{\rho^2}\left(\frac{\partial P}{\partial E}\right)^2\right]\frac{1}{K_S}. \tag{7}$$

The Grüneisen parameter $\gamma\equiv\rho^{-1}(\partial P/\partial E)_\rho$ is taken to be a function of density alone of the form

$$\gamma\rho^q=\gamma_0\rho_0^q=\text{constant}. \tag{8}$$

The quantities c, s, ρ, and U for the left and right states are given as input to the Riemann solver, which uses (3) and the one-dimensional Rankine-Hugoniot conservation laws to extrapolate the pressure, density, energy, and velocity of the solution without re-evaluating the equation of state. Given the simple linear form (3), pressure is quadratic in velocity:

$$P=P_0+\rho cU_P+\rho sU_P^2. \tag{9}$$

Equating pressure and velocity for the left and right materials amounts to simply solving a quadratic equation [e.g., see Ref. 24 (§2.1)]. This method takes advantage of the well-known result that release adiabats are nearly indistinguishable from reflected Hugoniots in the pressure-velocity plane.[1,24]

If the principal Hugoniot that acts as the reference curve of our Mie-Grüneisen equation of state has the form (3) and (9), if the left and right thermodynamic states (ρ_L,P_L,E_L) and (ρ_R,P_R,E_R) are equal to the centering point of that principal Hugoniot (ρ_0,P_0,E_0), and if the Riemann problem results in the formation of two shocks (i.e., $U_L>U_R$), then our approximate Riemann solver gives the exact solution. Our approximate method is also asymptotically correct in the limit of weak disturbances. In that asymptotic limit shocks are isentropic; thus, the use of a single quadratic $P(U)$ function to describe both shocks and rarefactions is appropriate (cf. Ref. 25).

In the case of strong shocks, the finite difference method will spread the shock onto several grids regardless of the precision of the Riemann solver.[26] We can therefore obtain the correct upwind and downwind quantities without accurately resolving the steep gradients between them.

A similar situation occurs when a strong rarefaction is formed. However, in that case the wave's intrinsic dispersion additionally acts to smooth the flow and improve the accuracy of our approximate method. Since the discretization of our grid automatically results in first-order errors near strong disturbances,[26] and since our approximate Riemann solver works well otherwise, an exact Riemann solver will not appreciably improve the resolution of our finite difference computation.

We use second-order operator splitting[27] to advance our two dimensional computational grid by a time step $2\Delta t$ by sequentially advancing one-dimensional strips of the grid by time steps Δt, alternating x and y sweeps at each time step. The one-dimensional grids are integrated with a second-order Godunov method.[28–31] Slope-limited interpolation is used to represent density, pressure, energy, and velocity as piecewise continuous functions in one dimension.[28,31] Characteristic tracing is then used to estimate the pressure, density, and velocity at the left and right boundaries of each cell at one half the one-dimensional time step $(t+\Delta t/2)$.[28] The Riemann problem is then solved at each cell edge in the one-dimensional strip using these time-centered, slope-limited, interpolated estimates of the left and right states. The solution of the Riemann problem determines the time-centered flux of the conserved quantities: mass, momentum, and energy. The new cell-centered quantities at $t+\Delta t$ are calculated in conservation form from those time-centered fluxes. The new two-dimensional solution, obtained in the sequence x-y-y-x, is a second-order accurate solution to the two-dimensional problem in regions of smooth flow.

The material interface boundary condition is neither strictly "slip" nor "stick" in our computation. On a length scale smaller than a single grid cell the material interface may be considered "stick" since, prior to the slope-limited interpolation step, a single velocity vector is used to characterize all material velocities within a given cell. However, adjacent cells may have different velocities and there is no restriction on the component of velocity tangential to the boundary between adjacent cells. Therefore, at length scales larger than a single cell the material interface boundary condition is "slip."

We explicitly track the interface between different materials with a volume-of-fluid interface tracking algorithm. However, for the purpose of finding a solution to the Riemann problem, the thermodynamic properties of those cells that contain more than one material are treated as an effective single fluid with isentropically averaged properties.[20,21] The effective single-fluid properties are used to set up and solve the Riemann problem as described above. However, at those cell edges separating two fluids or adjoining a multifluid cell the fluxes determined by the Riemann problem solution are modified before updating the cell-centered properties. The approximate location of the interface separating different materials is estimated using the first-order SLIC algorithm.[32] We note that second-order volume-of-fluid interface tracking algorithms are available,[33,34] but we use SLIC here since we have not yet programmed those second-order algorithms for cylindrical geometry. The time-centered velocity determined at the cell edge by the Riemann solver, together with the approximate location of the material interface, determines the mass flux of each individual material component through the cell edge. We then update the individual material properties in each cell using fluxes obtained from effective single fluid mixtures. At the end of each one-dimensional sweep, energy and volume are repartitioned adiabatically between each component in the multifluid cells. The objective of this step is to modify the volumes occupied by each phase, and modify their internal energies, such that energy and volume are conserved and each phase has the same final pressure. This is most accurately done by iteratively evaluating the equation of state, but that can be computationally very expensive. When the equation of state is not re-evaluated in this relaxation step, some residual pressure mismatch exists at the material interface. This can be seen as spurious closed contours in some plots of pressure shown below. If correctly done, no pressure discontinuity will exist in general at the material interfaces.

The two-dimensional conservative integrator just described is driven by an adaptive mesh refinement program (AMR).[35,36] This program employs a test to determine which regions of the problem domain would benefit from being solved on a finer grid. In the work presented here we used two criteria for deciding when to refine a grid cell. The first is that we refine to the maximum extent all cells that contain a material interface. (The maximum extent is a parameter supplied by the user at run time. In the computations shown here we allowed a maximum of 1 level of refinement with a refinement factor of 4 between the coarse and fine grids.) The second criterion is based on the use of Richardson extrapolation to estimate the local truncation error in the computed solution. This is accomplished by periodically comparing the solution on a grid advanced twice with time step Δt and then coarsened by a factor of two in each direction, with a coarsened grid advanced once with time step $2\Delta t$. In regions of smooth flow the difference between the solutions obtained on the two grids at each point is proportional to the local truncation error at that point. In addition, this procedure will generally predict a large error near discontinuities (e.g., shocks) in the flow. In the work presented here we found that we were able to obtain good results by only examining the difference in the values of density obtained on the two grids. Thus, if the material density in these two coarse test grids differed by some predetermined amount when normalized by the reference cell density, then the patch in space surrounding that reference cell was marked for computation on a finer grid. This test primarily identified shocks and steep rarefaction fans as regions requiring extra refinement. For the computations shown below we implemented this test every two time steps, and mark a cell for refinement if the normalized density difference exceeded 10^{-4}.

For simplicity, both fluid and solid phases are modeled in the hydrostatic limit. Strength effects are ignored. Consequently, phenomena such as elastic precursors will not occur in our computations. This non-hydrostatic behavior frustrated the original experimental efforts of Al'tshuler

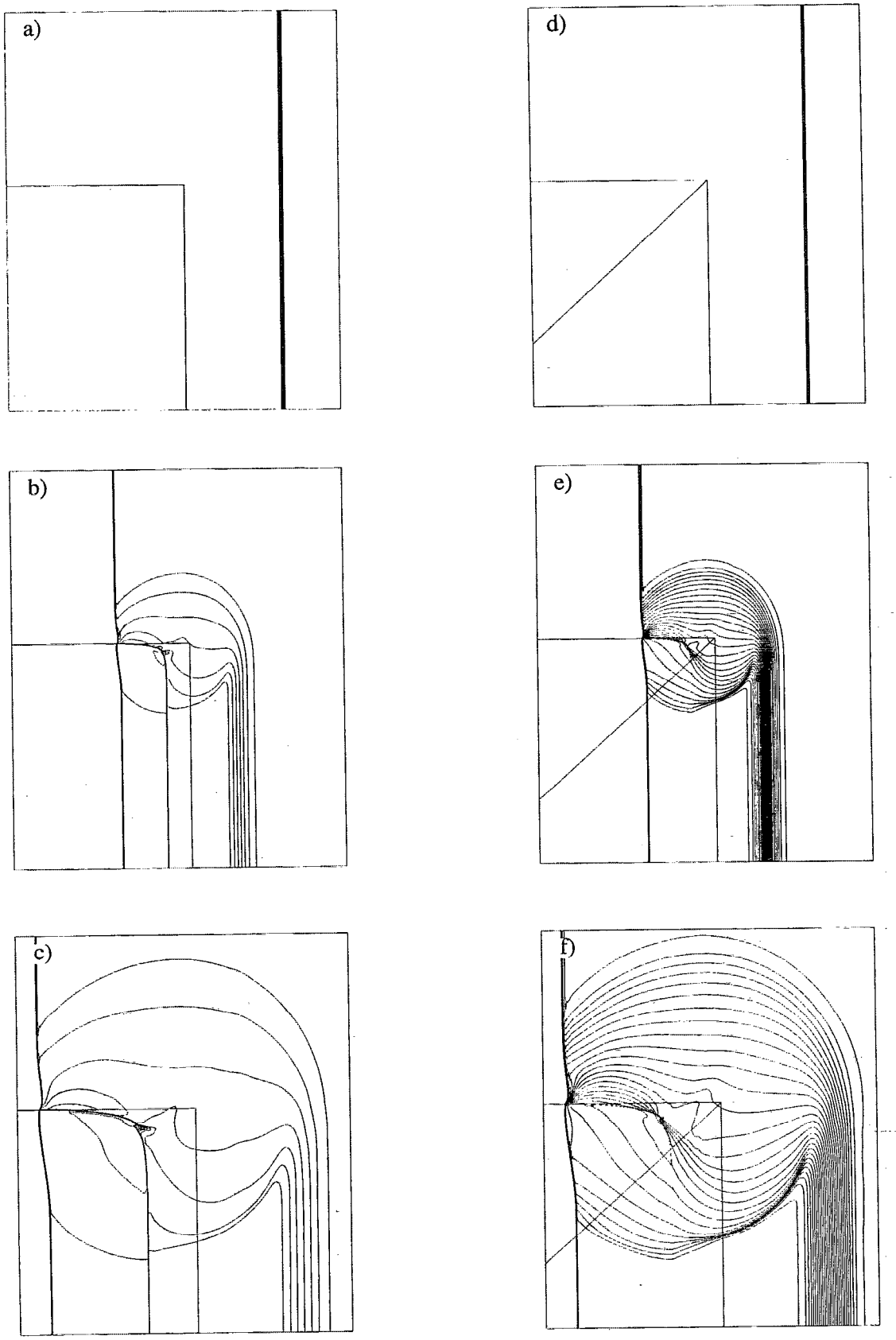

FIG. 4. A 90 GPa shock in molybdenum strikes a komatiite sample. (a)–(c) Density contours at 0.2 g/cc intervals at times −342 ns, 264 ns, and 560 ns after the shock first entered the liquid sample. (d)–(f) Pressure contours at 2 GPa intervals at times −342, 264, and 560 ns. (g)–(i) Regions selected by the AMR test for computation on a fine grid at times −342, 264, and 560 ns. The original material interface is shown as the box in the lower left hand corner of parts (a)–(f). Parts (d)–(f) also show the Al'tshuler *et al.* ray emanating from the corner of that box.

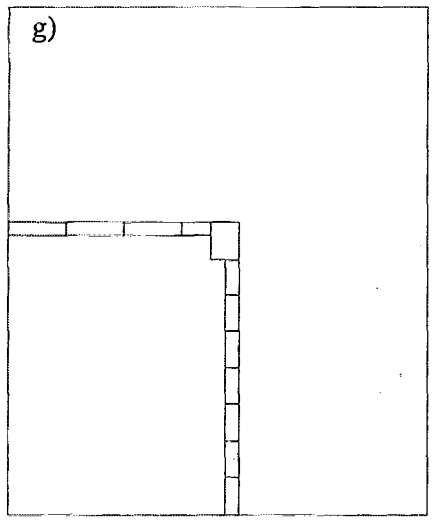

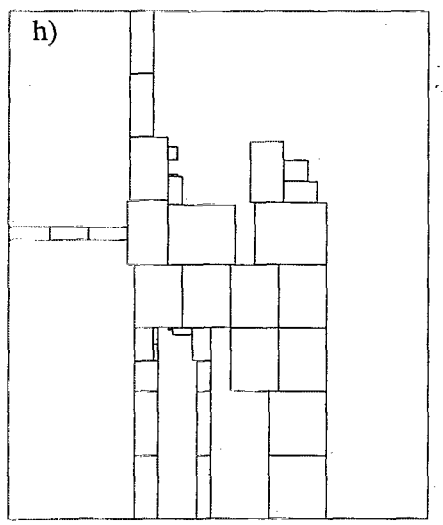

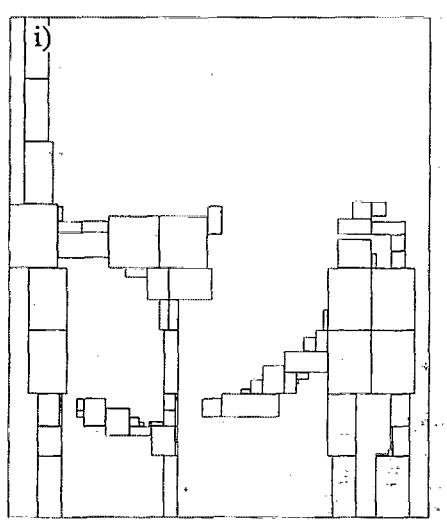

FIG. 4. (*Continued.*)

et al.[8] to obtain sound speed from measurements of α. However, under the conditions of the experiments we model below, the shear strength of the solid phase is much smaller than the hydrostatic pressure. Moreover, it is common to consider nonhydrostatic behavior as an additive perturbation to a nominally hydrostatic material response.[37]

III. RESULTS AND DISCUSSION

Figure 4 contains a series of density and pressure contours corresponding to a simulation of the most energetic experiment in Ref. 9 on a molten komatiite composition. The simulation begins with a 90 GPa left-traveling shock in molybdenum, and progresses until the shock transmitted in the komatiite has traveled about 3.55 mm: the thickness of the molten sample in the assembly illustrated in Fig. 2(a). Time $t=0$ corresponds to the arrival of the 90 GPa shock at the material interface. This computation was done in cylindrical coordinates: the bottom edge of the problem domain is the axis of symmetry.

When the incident shock first strikes the material interface, a planar 36 GPa shock is transmitted to the left into the komatiite, and a dispersive release fan is reflected to the right into the shocked molybdenum. At the corner, the incident shock is diffracted.

The original rectangular material interface is shown on these density and pressure contour plots. After refraction of the shock, the material interface is deformed by the expansion of the surrounding shocked molybdenum. That expansion is driven by the 54 GPa pressure difference between the 90 GPa shocked molybdenum and the 36 GPa shocked sample. That expansion is seen as the "circular" rarefaction front (clockwise from 9 o'clock to 3 o'clock), and drives a corresponding "circular" compressional wave into the released molybdenum (from 3 o'clock to 6 o'clock), and into the shocked molten komatiite (from 6 o'clock to 9 o'clock). These "circular" waves are actually toroidal in 3 dimensions.

The curved compressional wave front traveling into the released molybdenum does appear to have steepened into a shock, judging from the stacking up of pressure contours on the leading edge of that wave system. However, the curved compressional wave front does *not* steepen into a shock in the komatiite sample. Its leading edge therefore travels at the 36 GPa bulk sound speed of that material, and the intersection of the expanding wave front with the otherwise planar transmitted shock lies on the Al'tshuler *et al.* ray. That ray, which emanates from the initial position of the material interface corner, is shown on the pressure contour plots. Below that ray, the transmitted shock is planar. Above it, the shock is curved by interaction with the curved compressional wave front.

Those regions of the computational grid that were selected by the AMR error estimation routine for additional refinement are shown in Figs. 4(g)–4(i). These are not grid cells, but regions where the original coarse grid computation was done on a 4-times finer grid. The original coarse grid for this problem was 174 by 216.

Figure 5 illustrates the material velocity structure of the simulation. The location of the deformed material interface is immediately obvious in contours of Z and R velocity. That is because, although there is no jump in velocity *normal* to the interface, there is no restriction on

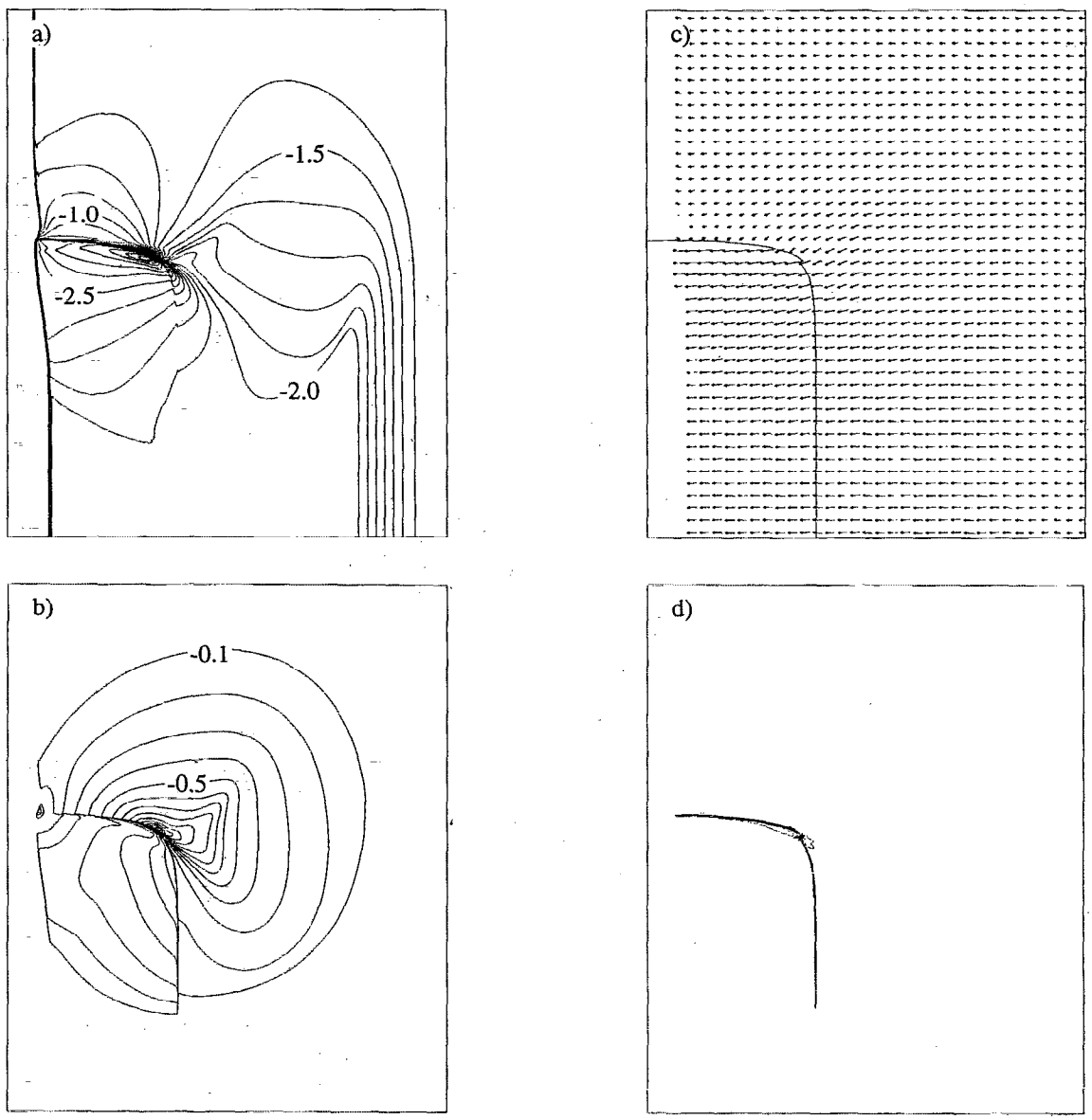

FIG. 5. Material velocity for same problem as Fig. 4. Z velocity, which ranges from -3.23 km/s to 0, is contoured at 0.1 km/s intervals. R velocity ranges from -1.41 to 0.31 and is contoured at 0.1 km/s intervals (from -1.4 to -0.1 and from 0.1 to 0.3). (c) illustrates the velocity vectors in relation to the material interface. (d) is the vorticity $\nabla\times\mathbf{v}$, which ranges from -58 to 87 s^{-1}.

the velocity jump in the *tangential* direction. Apparently, within the region bounded by the "circular" wave front the molybdenum and komatiite are sliding against one another at their interface. This is most obvious in Fig. 5(c) where the Z velocity can be seen to jump dramatically across the horizontal part of the material interface. An R-velocity discontinuity across the vertical part of the interface is more easily seen in Fig. 5(b). This sliding material interface can also be seen in a plot of vorticity [Fig. 5(d)]. The deformed material interface is drawn on Fig. 5(c), where it can be seen to have torn near the corner.

An unexpected feature of the komatiite computation is that at the material interface, the leading edge of the komatiite shock leads the leading edge of the molybdenum shock: the shock front has a "Z"-shaped profile. This has been seen before in gas dynamics studies of anomalous refraction at a sloped material interface.[38] It occurs when the shock impedance of the the oblique transmitted wave is larger than that of the planar incident wave.[19] Here, wave impedance is defined as $Z_i=\rho_i U_i/\cos\beta_i$: the mass flux convected through the wave divided by the cosine of the angle the shock makes with the *deflected* material interface. This is the natural generalization of impedance to oblique shock waves.[15] It is analogous to the generalization of the acoustic impedance to effective acoustic impedance. However, in this particular case the condition $(\rho U)_{\text{komatiite}} > (\rho U)_{\text{molybdenum}}$ is not satisfied when evaluated in the steady regions away from the material interface since both the shock velocity and density of komatiite are smaller than the corresponding quantities in molybdenum.

For comparison, a simulation of molybdenum-encased Mid-Ocean Ridge Basalt (MORB), corresponding to the

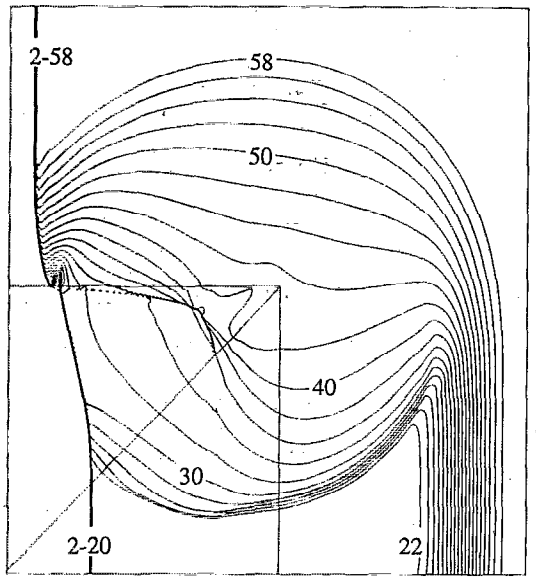

FIG. 6. MORB in molybdenum at 745 ns. The domain is 9.78 by 10.86 mm, and the initial shock in molybdenum is 60.8 GPa. Pressure contours are shown from 2 to 58 GPa in steps of 2.

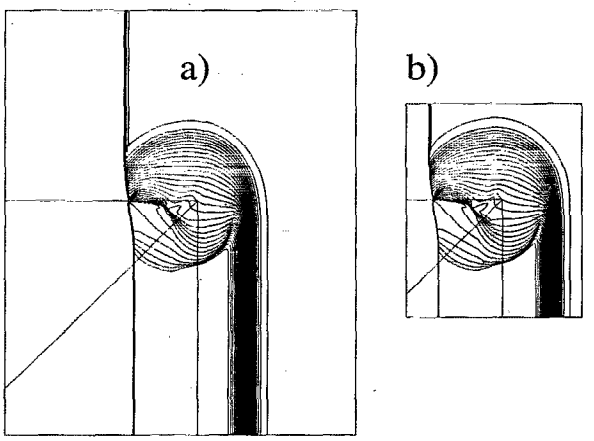

FIG. 7. Self-similarity of Cartesian system illustrated by pressure contours (at 2, 4, 6, ..., 98 GPa) at times 250 ns (a) and 500 ns (b). The materials are anorthite and molybdenum. The post-shock anorthite pressure is 38.8 GPa.

most energetic experiment of Ref. 39, is shown in Fig. 6. The contour plot of pressure clearly shows a complicated shock structure where the MORB shock, deflected by the corner signal, is bent forward (to the left) and continues smoothly as a shock in the molybdenum that lies to the right of the leading shock in that material. The two shocks are joined by a collection of waves in the molybdenum.

The MORB shock never leads the molybdenum shock, in contrast to the komatiite computation. Also, unlike the komatiite computation the curved compressional wave in the molybdenum does not appear to have steepened into a shock. However, as with the komatiite computation, the leading disturbance in the liquid sample travels with the sound speed and obeys the Al'tshuler *et al.* rule. In fact, computations for molten diopside and anorthite compositions, and a diopside-anorthite composition mixture are all consistent with the disturbance being acoustic.

The position of the material interface can be seen in pressure contours plots because of the numerous closed contours that occur there. This artifact of the multifluid algorithm scales with the grid size: these spurious closed contours can be made arbitrarily small if a sufficiently fine grid is used.

An indication of the precision of our computations is the self-similarity that can be seen in Cartesian coordinates. In cylindrical coordinates there is a length scale to the problem (r_0, the radial coordinate of the undeformed corner), and so the problem is not self-similar. In Cartesian coordinates, however, there is no length scale. The solution at $(x/t, y/t)$ should be independent of t for all $t > t_0$, where t_0 is the moment when the shock first reaches the corner (0,0). Figure 7 shows a Cartesian computation for molten anorthite (corresponding to the most energetic experiment in Ref. 12) at times 250 ns and 500 ns after the incident shock has collided with the material interface. These two pressure contour plots are scaled by $1/t$. So scaled, the two plots are nearly identical. Note that in this anorthite computation the shock front exhibits the anomalous "Z"-shape seen for the molten komatiite (Fig. 4). However, in this case the perturbed anorthite shock does not lead the undisturbed incident shock in the molybdenum.

Our computations support the use of the Al'tshuler *et al.* design rule [Eq. (1)] for those molten silicate compositions studied in Refs. 9–13. If we assume that this rule is also valid for molten silicate compositions that may be studied in the future, then we can extend the Al'tshuler *et al.* model (Fig. 1) to include the acoustic propagation of edge effects in the cap of the molybdenum sample container. In order to account for the container's nonhydrostatic behavior, we use an Al'tshuler *et al.* type calculation for the propagation of edge signals in the cap, but use the longitudinal wave speed v_p instead of the slower bulk sound speed c.[40] This calculation, schematically illustrated in Fig. 8, requires knowledge of the bulk sound speed in the shocked liquid, and of the longitudinal sound speed in the metal cap after being shocked by the liquid.[41]

IV. CONCLUSIONS

We have extended a high-order multifluid Godunov algorithm for gas dynamics to include the hydrostatic Mie-Grüneisen equation of state. We have used this new algorithm to model experiments in which molybdenum-encased molten silicates are shocked to determine their equations of state. The results of our computations suggest that the degradation of the initially planar silicate shock by edge effects may be successfully modeled by the Al'tshuler *et al.* formula. Therefore, the aspect ratios of the samples used in Refs. 9–13 are adequate, and the application of the one-dimensional Rankine-Hugoniot relations to those experiments is appropriate. The equations of state presented by those authors are therefore internally consistent with the assumptions required by their analysis.

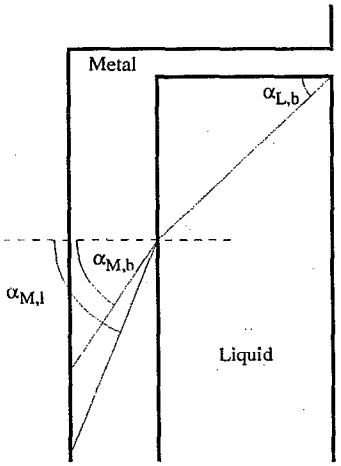

FIG. 8. Estimation of aspect ratio for composite sample assembly illustrated in Fig. 2 and used in experiments (Refs. 9–13) . $\alpha_{L,b}$ is calculated from Eq. (1) using the bulk sound speed of the liquid. $\alpha_{M,b}$ and $\alpha_{M,l}$ are calculated with the bulk and longitudinal sound speeds, respectively, of the metal. The metal thickness has been exaggerated for clarity.

Although in theory the measurement of the edge effect may be used to deduce the high pressure sound speed, the strength of the shock front disturbance asymptotically approaches zero at the leading acoustic wave. Therefore, the Al'tshuler *et al.* angle α is very difficult to detect experimentally. Any measured shock front disturbance will likely give only a lower bound on α and thus a lower bound on the high pressure sound speed. Forward modeling of the entire shock arrival profile, using high-resolution numerical computations of the type shown here, might be successfully applied to deduce a sound speed. However, any such model sound speed will be sensitive to the specific equation of state approximations used by the computation.

ACKNOWLEDGMENTS

We thank P. Colella, H. Glaz, and R. Ferguson for sharing their manuscript with us prior to its submission for publication. We are also grateful to A. Bourlioux and P. Colella of U. C. Berkeley for making this collaboration possible, and for many helpful discussions. GHM thanks W. Nellis of the Lawrence Livermore National Laboratory for bringing this problem to his attention.

Work of the first author was supported by the National Science Foundation (NSF) under grant EAR-9219092. Work of the second author was supported by NSF under grant DMS-9104472. Work at U.C. Berkeley was supported by DARPA and the NSF under grant DMS-8919074. Computational support was provided by the NSF San Diego Supercomputer Center and the National Center for Supercomputing Applications, University of Illinois at Urbana-Champaign.

[1] J. M. Walsh and R. H. Christian, Phys. Rev. **97**, 1544 (1955).
[2] W. J. M. Rankine, Philos. Trans. R. Soc. London **160**, 277 (1870).
[3] H. Hugoniot, J. École Polyt. Paris **57**, 3 (1887).
[4] H. Hugoniot, J. École Polyt. Paris **58**, 1 (1889).
[5] C. E. R. III, M. G. Silbert, and B. C. Diven, J. Appl. Phys. **48**, 2860 (1977).
[6] H. K. Mao, P. M. Bell, J. W. Shaner, and D. J. Steinberg, J. Appl. Phys. **49**, 3276 (1978).
[7] H. K. Mao, J. Xu, and P. M. Bell, J. Geophys. Res. **91**, 4673 (1986).
[8] L. V. Al'tshuler, S. B. Kormer, M. I. Brazhinik, L. A. Vladimirov, M. P. Speraanskaya, and A. I. Funtikov, Sov. Phys. JETP **11**, 766 (1960).
[9] G. H. Miller, E. M. Stolper, and T. J. Ahrens, J. Geophys. Res. **96**, 11,831 (1991).
[10] S. M. Rigden, T. J. Ahrens, and E. M. Stolper, Science **226**, 1071 (1984).
[11] S. M. Rigden, T. J. Ahrens, and E. M. Stolper, J. Geophys. Res. **93**, 367 (1988).
[12] S. M. Rigden, T. J. Ahrens, and E. M. Stolper, J. Geophys. Res. **94**, 9508 (1989).
[13] L. R. Rowan, T. J. Ahrens, and E. M. Stolper, EOS Trans. Amer. Geophys. Union, **72**, 548 (1991) (abstract).
[14] P. A. Voinovich, A. I. Zhmakin, and A. A. Fursenko, Sov. Phys. Tech. Phys. **33**, 748 (1988).
[15] L. F. Henderson, J. Fluid Mech. **198**, 365 (1989).
[16] J. W. Grove and R. Menikoff, J. Fluid Mech. **219**, 313 (1990).
[17] L. F. Henderson and E. G. Puckett (unpublished).
[18] L. F. Henderson, E. G. Puckett, and P. Colella, in *Shock Waves*, edited by K. Takayama (Springer, New York, 1992), pp. 283–286.
[19] E. G. Puckett, L. F. Henderson, and P. Colella (unpublished).
[20] P. Colella, H. M. Glaz, and R. Ferguson (unpublished, 1993).
[21] E. G. Puckett and J. S. Saltzman, Physica D **60**, 84 (1992).
[22] R. Menikoff and B. J. Plohr, Rev. Mod. Phys. **61**, 75 (1989).
[23] E. Grüneisen, in *Handbuch der Phys, Bd. 10* (Springer, Berlin, 1927), pp. 1–52.
[24] T. J. Ahrens, in *Geophysics, Laboratory Measurements*, Vol. 24-Part A of *Methods of Experimental Physics*, edited by C. G. Sammis and T. L. Henyey (Academic, New York, 1987), pp. 185–235.
[25] S. B. Segletes, J. Appl. Phys. **70**, 2489 (1991).
[26] P. R. Woodward, in *Astrophysical Radiation Hydrodynamics*, edited by K.-H. Winkler and M. Norman (Reidel, Boston, 1986).
[27] G. Strang, Num. Math. **6**, 37 (1964).
[28] P. Colella, SIAM J. Sci. Stat. Comput. **6**, 104 (1985).
[29] P. Colella and H. M. Glaz, J. Comput. Phys. **59**, 264 (1985).
[30] P. Colella and P. R. Woodward, J. Comput. Phys. **54**, 174 (1984).
[31] B. van Leer, J. Comput. Phys. **32**, 101 (1979).
[32] W. F. Noh and P. R. Woodward, in *Lecture Notes in Physics; 59*, edited by A. I. van der Vooren and P. J. Zandbergen (Springer, New York, 1976), pp. 330–340.
[33] E. G. Puckett, in *Proceedings of the 4th International Symposium on Computational Fluid Dynamics*, edited by H. Dwyer (U. C. Davis, Davis, CA, 1991), pp. 933–938.
[34] J. E. Pilliod and E. G. Puckett (unpublished).
[35] M. J. Berger and P. Colella, J. Comput. Phys. **82**, 64 (1989).
[36] J. B. Bell, M. J. Berger, J. S. Saltzman, and M. L. Welcome, SIAM J. Sci. Stat. Comput. (to be published).
[37] J. A. Zukas, in *Impact Dynamics*, edited by J. A. Zukas, T. Nicholas, H. Swift, L. B. Greszczuk, and D. R. Curran (Wiley, New York, 1982), pp. 367–418.
[38] A. M. Abd-el-Fattah and L. F. Henderson, J. Fluid Mech. **86**, 15 (1978).
[39] L. R. Rowan, Ph.D. thesis, California Institute of Technology, 1993.
[40] R. G. McQueen, in *High Pressure Equations of State: Theory and Applications*, Vol. 113 of *Proceedings of the International School of Physics "Enrico Fermi,"* edited by S. Eliezer and R. A. Ricci (North-Holland, New York, 1991), pp. 101–216.
[41] T. S. Duffy, Ph.D. thesis, California Institute of Technology, 1992.